ADVANCED FUNCTIONAL MATERIALS
www.afm-journal.de

www.MaterialsViews.com

Structure-Invertible Nanoparticles for Triggered Co-Delivery of Nucleic Acids and Hydrophobic Drugs for Combination Cancer Therapy

Kai Wang, Qida Hu, Wei Zhu, Mengmeng Zhao, Yuan Ping, and Guping Tang**

Here, a new type of structure-invertible, redox-responsive polymeric nanoparticle for the efficient co-delivery of nucleic acids and hydrophobic drugs in vitro and in vivo is reported for the first time, to combat the major challenges facing combination cancer therapy. The co-delivery vector, which is prepared by conjugating branched poly(ethylene glycol) with dendrimers of two generations (G2) through disulfide linkages, is able to complex nucleic acids and load hydrophobic drugs with high loading capacity through structure inversion. The cleavage of disulfide linkages at intracellular glutathione-rich reduction environment significantly decreases the cytotoxicity, and promotes more efficient drug release and gene transfection in vitro and in vivo. The co-delivery carrier also displays enhanced endosomal escape capability and improved serum stability in vitro as compared with G2, and exhibits prolonged residence time and stronger transfection activity in vivo. Most importantly, co-delivery of doxorubicin (DOX) and B-cell lymphoma 2 (Bcl-2) small interfering RNA (siRNA) exerts a combinational effect against tumor growth in murine tumor models in vivo, which is much more effective than either DOX or Bcl-2 siRNA-based monotherapy. The structure-invertible nanoparticles may constitute a promising stimuli-responsive system for the efficacious co-delivery of multiple cargoes in future clinical applications of combination cancer therapies.

1. Introduction

In the past few years, one of the most important developments in drug delivery is to load and deliver two or multiple drugs of complementary effects with a single vehicle to maximize the benefit of combination therapies.[1–5] This delivery strategy, termed as co-delivery, was reported to enhance the efficiency of delivering two drugs to the same cell population by at least one order of magnitude when compared with delivering them in two separate carriers.[6] Currently, co-delivery of chemotherapeutic drugs and nucleic acids with a wide range of therapeutic option is extensively explored for the combination therapy of cancer, and these combined therapies promote combination or synergism among drugs against cancer cells and suppress drug resistance through distinct mechanisms of action, thereby inhibiting tumor progression. One of the major challenges facing such combination therapies is the requirement of a safe and efficient carrier system for the simultaneous co-delivery of drugs and nucleic acids to pass through multiple physiological barriers. Currently, there are a few types of co-delivery vectors available, such as polymeric micelles,[2,7–9] cationic supramolecular nanoparticles,[10–15] liposomes,[16–18] mesoporous silica nanoparticles,[19–21] dendrimers,[22–25] and other organic and inorganic materials.[26–28] Cationic polyamidoamine (PAMAM) dendrimers are emerging as promising vectors for the simultaneous co-delivery of chemotherapeutics and nucleic acids due to their controllable physicochemical properties and desirable biological features.[29] The well-defined nanoscaled molecular architecture, unique supramolecular and interfacial features, as well as untoward immunogenicity in vivo, have made PAMAM dendrimers as promising nanocarriers for the co-delivery of bioactive agents.[29] Low-molecular-weight hydrophobic drugs typically interact with PAMAM dendrimer via hydrophobic interactions between dendrimer cavities and drugs, while the presence of a large number of

K. Wang, M. Zhao, Prof. G. Tang
Institute of Chemical Biology and Pharmaceutical Chemistry
Zhejiang University
Hangzhou 310028, China
E-mail: tangguping@zju.edu.cn

Q. Hu
Department of Hepatobiliary and Pancreatic Surgery
The Second Affiliated Hospital
Zhejiang University School of Medicine
Hangzhou 310009, China

Dr. W. Zhu
Molecular Nanofabrication Group
MESA+ Institute for Nanotechnology
University of Twente
7500 AE, Enschede, The Netherlands

Dr. Y. Ping
Department of Chemical and Biomolecular Engineering
The University of Melbourne
Victoria 3010, Australia
E-mail: pingyuan7@gmail.com

DOI: 10.1002/adfm.201403921

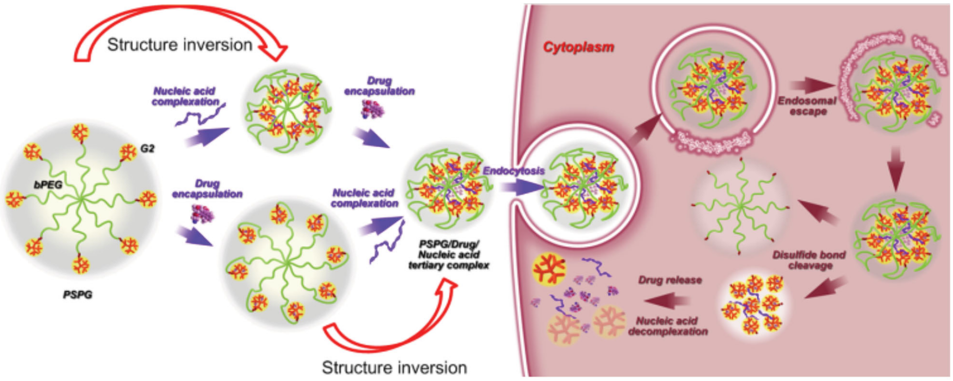

Figure 1. Schematic illustration of drug-loaded, nucleic acid–complexed co-delivery vectors and their structure inversion after nucleic acid complexation. Intracellular delivery process of PSPG/drug/nucleic acid tertiary complexes indicates that PSPG exhibited enhanced endosomal escape and intracellular degradation that facilitates efficient drug and nucleic acid release in the cytosol.

surface primary amine groups provides the electrostatic force to interact with negatively charged nucleic acids. Therefore, as a drug delivery carrier, PAMAM dendrimers are readily used for the simultaneous loading of hydrophobic drugs and nucleic acids.

Nevertheless, PAMAM dendrimers are involved with a few challenges as co-delivery vectors. Although low generation dendrimers are of low cytotoxicity toward transfected cells, their gene transfection efficiency is generally low as well when compared with high generations due to inefficient endosomal escape capability.[30] In contrast, PAMAM dendrimers with high gene transfection efficacy generally induce serious cytotoxicity to transfected cells.[31] Some efforts and progress have been made recently to break up the correlation between delivery efficacy and cytotoxicity for cationic dendrimer vectors. For example, disulfide crosslinked low generation dendrimers were found to possess low cytotoxicity and high gene transfection efficacy in vitro due to the reduced cytotoxicity and enhanced DNA release through the cleavage of disulfide bonds.[32] Additionally, the drug loading capacity is also highly dependent on the generation number: lower generation dendrimers are less capable of encapsulating hydrophobic drugs into interior cavities than higher generation ones, thereby possessing low loading capacity.[33] Higher generation dendrimers which typically exhibit densely packed surface are able to form enclosed internal voids to effectively encapsulate and retain guest molecules.[34] Moreover, the efficiency of dendrimer-mediated co-delivery was commonly suffered by inadequate drug release into the cytosol and serum stability, which often constitute the main obstacles for successful combination therapy.[30,31,34] Last but not least, PAMAM in vivo stability is poor due to the nonspecific interaction between positively charged dendron and negatively charged plasma protein, leading to the aggregation of particles and poor cellular uptake. To overcome this problem, various efforts have been undertaken to enhance serum stability in vitro and in vivo.[35–38] Although many efforts have been undertaken to overcome these problems, it is still of great challenge to integrate multifunctional properties into a single co-delivery vehicle that can address all these issues.[32,35–38]

The motivation behind us developing dendrimer-based polymeric vectors is to overcome aforementioned obstacles in the co-delivery application. To this end, we herein disclose that structure-invertible, redox-responsive low generation dendrimers covalently assembled from branched polyethylene glycol (bPEG) networks with disulfide linkages act as an efficient vector to simultaneously deliver nucleic acids (either plasmid DNA (pDNA) or small interfering RNA (siRNA)) and hydrophobic drugs in vitro and in vivo. This new co-delivery carrier is expected to provide high drug loading, enhanced endosomal escape, low cytotoxicity, and improved serum stability. It is also expected to constitute a new type of stimuli-responsive system for the efficacious co-delivery of chemotherapeutic drugs and nucleic acids for combination cancer therapy. To the best of our knowledge, this is the first report of a dynamic, structure-invertible co-delivery nanocarrier that is able to simultaneously deliver nucleic acids and hydrophobic drugs in an efficient manner for combination cancer treatment in vivo.

2. Results and Discussion

2.1. Co-Delivery Carrier Preparation and Cargo Loading

The most frequently used co-delivery vectors such as nanoscaled liposomes, micelles, and supramolecular nanoparticles commonly suffer from poor in vivo stability, leakage of encapsulated drugs, and limited loading capacity.[39–41] Although mesoporous silica shows extraordinary capacity of drug loading and better stability, in vivo toxicity and biodegradability is still a major concern for the clinical translation.[42] Therefore, it is still of great significance to explore highly efficient co-delivery vectors with low toxicity for combination cancer therapy. As shown in **Figure 1**, the redox-responsive bPEG/dendrimer hybrid polymer possesses an interior hydrophilic, nonfouling bPEG arm and several low generation cationic PAMAM terminals that are linked by disulfide linkers. Our design consideration is that while PAMAM interior provides cavities to host hydrophobic drugs, the surface primary amines are able to interact with nucleic acids by electrostatic force. The neutral bPEG part not only provides a shielding layer to prevent nonspecific serum interactions, but also serves as a hydrophilic architecture

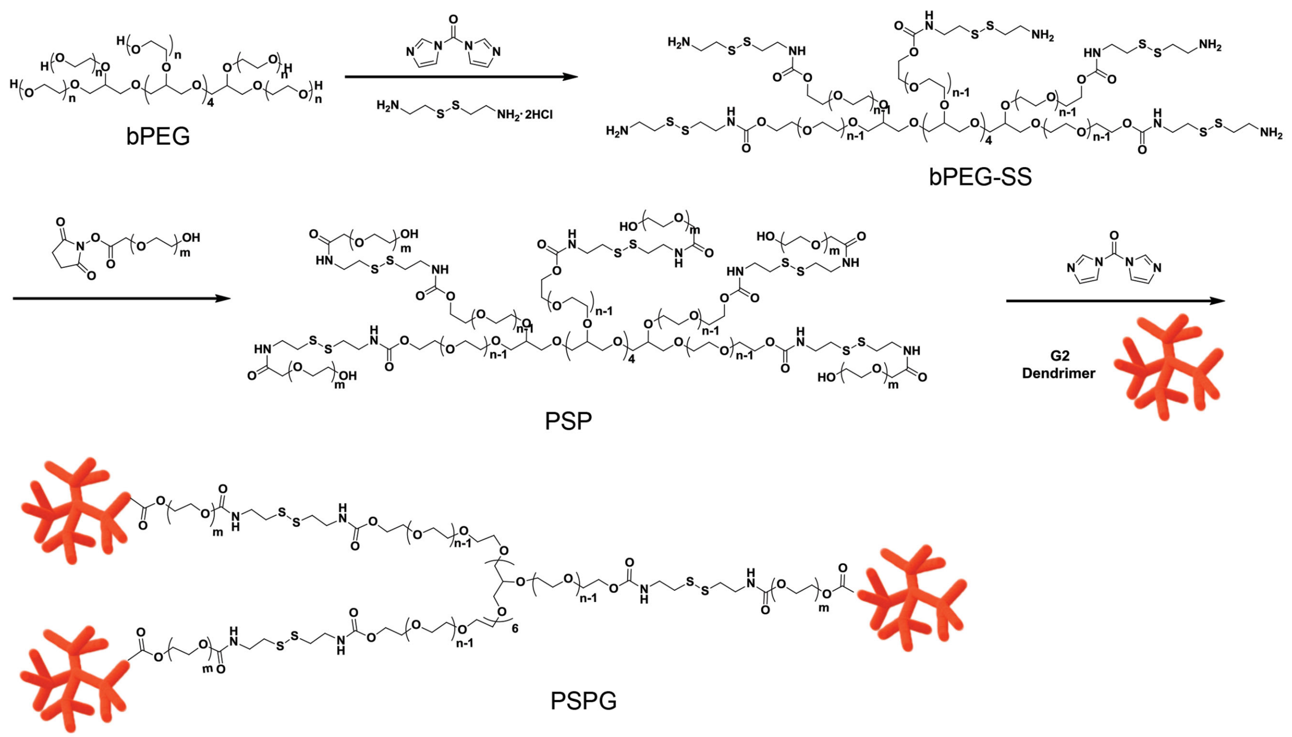

Scheme 1. Synthesis route of PSPG polymer.

to enhance drug loading capacity by modulating the conformation of internal voids. Additionally, bPEG also offers a branched network to assemble low generation dendrimers to mimic high generation dendrimers through redox-responsive disulfide bonds in order to enhance endosomal escape capability. These disulfide linkages that are readily cleaved by intracellular glutathione (GSH) ensure the disassembly of low generation dendrimers from bPEG network through thiol–disulfide exchange. The detachment of G2 moieties from bPEG not only decreases the cytotoxicity, but also promotes more efficient nucleic acid release. As a consequence, it is expected that a more effective and safer co-delivery may be achieved by taking advantages of special features of low generation dendrimers while merging desirable properties of PEG and thiol–disulfide chemistry. One of the interesting properties we found in this particular structure is that although interior bPEG was initially embedded by PAMAM moiety, such a structure inverted dramatically as an exterior bPEG/interior G2 structure upon DNA or siRNA complexation. The structure inversion of nanoparticles surprisingly results in a hollow interior structure, which is capable of hosting hydrophobic drugs primarily via hydrophobic interaction. Therefore, hydrophobic drugs can be loaded within both intramolecular void of G2 dendrimers and newly formed cavities, thus greatly enhancing the loading capacity of co-delivery vectors. These special features also greatly improve co-delivery performance as demonstrated in our current study. As compared to other co-delivery nanoparticles, the current co-delivery system is able to afford high capacity of hydrophobic drug loading, offer stimuli-responsive features for triggered drug release and gene transfection, and exhibit low in vivo cytotoxicity and enhanced serum stability.

We thus synthesized a series of redox-responsive PEG-modified dendrimers bearing different dendrimer density to retain and exploit the properties of both PEG and low generation dendrimer vectors (**Scheme 1**). The synthesis route of G2 dendrimers with the generation number of 2 is shown in Figure S1 (Supporting Information). The bPEG was first modified with cysteamine via 1,1′-carbonyldiimidazole (CDI)-mediated coupling reaction to introduce disulfide bond into the bPEG terminal. The resulted amine-terminated bPEG (bPEG-SS) was further conjugated with an amine-reactive, heterofunctional linear PEG (lPEG) to give bPEG-SS-lPEG (PSP). Finally, the hydroxyl groups at the terminal bPEG-SS-lPEG were further reacted with primary amines of G2 through CDI-mediated coupling reaction to yield the final product, bPEG-SS-lPEG-G2 (PSPG). The chemical structure of PSPG was characterized by proton nuclear magnetic resonance (^{1}H NMR) spectroscopy (**Figure 2**). While the typical proton signals attributed to bPEG were well observed, the successful introduction of disulfide bonds from bPEG-SS could be confirmed from the proton signals at δ2.7–2.9 ppm, which are associated with methylene proton in the vicinity of disulfide bonds from cystamine moiety. In the spectrum of PSP, the additional singlet at 4.0 ppm associated with protons in the vicinity of carbamate linkage as well as enhanced peak intensity from the methylene protons of lPEG demonstrates that the successful conjugation of lPEG segments. The newly formed characteristic singlet appeared between 1.80 and 2.30 ppm can be ascribed to methylene protons from G2 dendrimers in PSPG spectrum. By controlling the feeding ratio between G2 and PSP, PSPGs with G2 density from 2 to 8 mol per bPEG molecule (denoted as PSPG2, PSPG4, PSPG6, and PSPG8) were obtained (Figure S2,

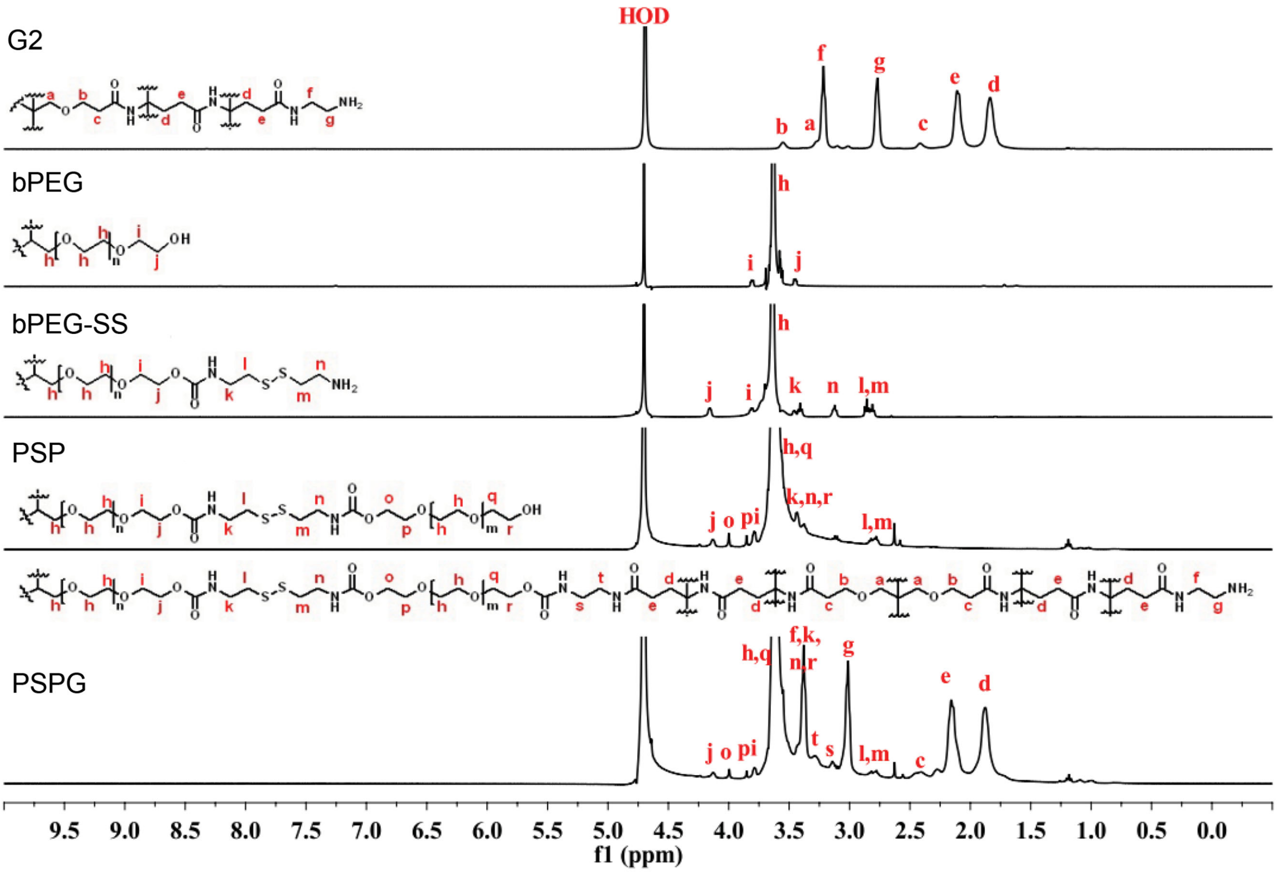

Figure 2. ^{1}H NMR spectrum of dendrimer G2, bPEG, bPEG-SS, PSP, and PSPG in D_2O.

Supporting Information). To demonstrate the PSPG inversion after cargo loading, X-ray photoelectron spectroscopy (XPS) C 1s core-level spectra of the PSPG6 and PSPG6/doxorubicin (DOX)/DNA were examined (**Figure 3**). The C 1s core-level spectrum of PSPG could be curve-fitted into three peak components with binding energies (BEs) at about 284.7, 285.9, and 287.8 eV, attributable to the C—H/C—C, C—N, and C=O species, respectively.[43] The C 1s core-level spectrum of PSPG/DOX/DNA could be curve-fitted by two peak components with BEs at about 284.5 and 286 eV, attributable to the C—H/C—C and C—O, respectively.[44] Furthermore, the O 1s core-level spectrum of PSPG could be curve-fitted by two components with BEs at about 531.4 and 532.9 eV, which is ascribed to C=O and C—O. Only C—O peak at 532.8 eV is available while C=O peak completely disappears after cargo loading. These XPS spectra provide most direct evidence that initial buried PEG networks invert to the surface of PAMAM nanoparticles after complexation with DNA. Concomitantly, Fourier transform infrared (FT-IR) spectroscopy indicates that the intensity of major characteristic peaks of PSPG6 associated with G2 moiety has dramatically decreased after cargo loading, whereas the intensity of absorption peaks in 2884 and 1103 cm^{-1} significantly increases, due to the asymmetric stretching vibration of C—H and C—O—C from the repeating units of the PEG, respectively (Figure S3, Supporting Information). All these data suggest that PEG has been reversibly exposed to the surface of PSPG. Based on the above information, the mechanism of structure inversion is proposed as follows: when negatively charged pDNA electrostatically interacts with the cationic PSPG6, pDNA condensation, which is driven by an entropy gain upon counterion release, occurs. Concomitantly, the electrostatic interactions also drive the formation of nanoscaled PSPG/DNA complexes.[45] This process also drives the cationic G2/DNA moiety into the inner part of polyplexes, whereas the neutral PEG blocks orientate toward the surface of nanoparticles.[46,47] The flexible G2 dendrimers may probably be subjected to supramolecular arrangements in response to hydrophobic interactions,[48] thus forming interior hydrophobic cavities.

2.2. Biophysical Properties of Structure-Invertible Nanoparticles

The morphology of the PSPG6, PSPG6/DNA complexes, and PSPG6/DNA/DOX complexes was characterized by transmission electron microscopy (TEM), energy-dispersive X-ray (EDX) spectroscopy, and confocal laser scanning microscopy (CLSM) (**Figure 4**). TEM indicates that the native PSPG6 is spherical particles with rough surfaces (Figure 4a,e), and is able to self-assemble into spherical, hollow nanoparticles after DNA complexation (Figure 4b,f and Figure S4, Supporting Information). The formation of hollow structure is probably due to the inter- or intramolecular rearrangement of hydrophobic cavities of G2

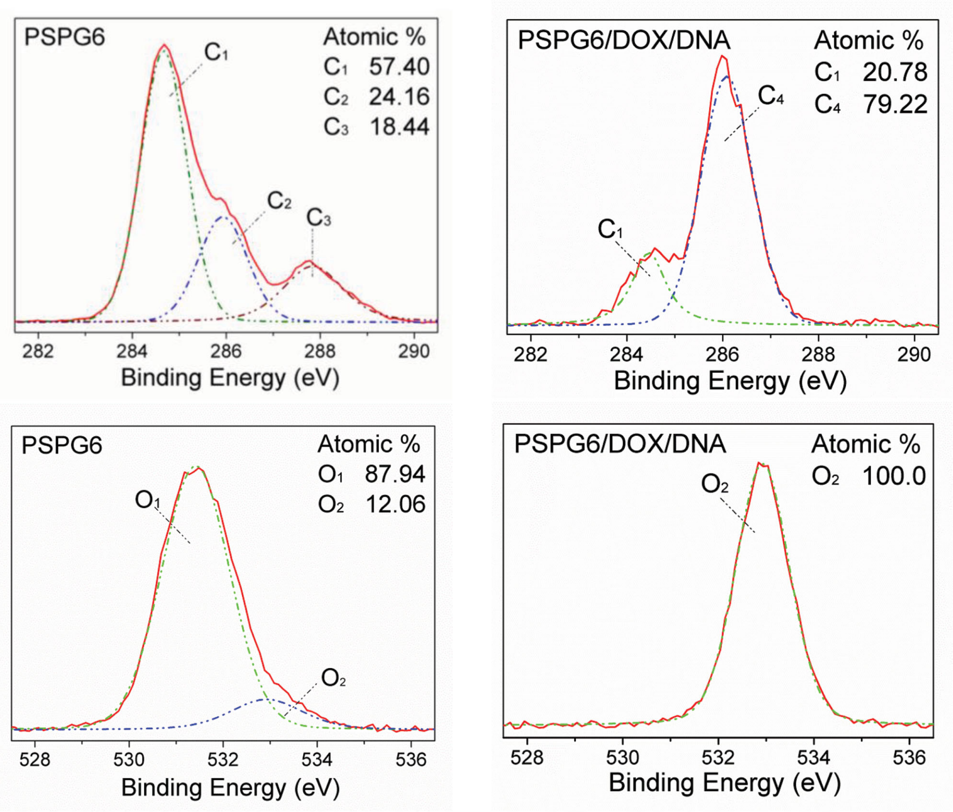

Figure 3. XPS survey C 1s and O 1s core-level spectra acquired from the surface of PSPG6 and PSPG6/DOX/DNA complexes.

through structure inversion (Figure S5, Supporting Information). During this process, either one PSPG molecule inverts as a single nanoparticle (intramolecular rearrangement, Figure 1), or multiple PSPG molecules invert and assemble into a single nanoparticle (intramolecular rearrangement, Figure S1a, Supporting Information). As a consequence, the size distribution of PSPG6/DNA seems to be slightly polydisperse. DOX could be loaded within the interior cavities of PSPG6 through hydrophobic interaction (Figure 4c,g), and it was clearly observed from TEM that the central core was even darker than the peripheral areas. The DOX-loaded, DNA-complexed PSPG6 nanoparticle exhibits a "core–shell" structure (Figure 4d,h and Figure S4, Supporting Information), where the core is full of DOX and the shell is made of PSPG6/DNA complexes. This hollow structure of PSPG6/DNA nanoparticles characterized by EDX mapping analysis demonstrates that the phosphorus (from DNA) distribution patterns matched well with high-angle annular dark-field images (HAADF) (Figure 4i–k). As G2 moiety in the terminal of PEG network is responsible to complex pDNA, the resulted PSPG6/DNA complexes probably form a bilayered shell structure. The exterior layer of the shell is PEG surface, whereas the interior layer of the shell is composed of G2/DNA complexes. During PSPG6-DNA self-assembling process, the void spaces within G2 dendrimers probably form either a single or a multicompartment cavity, allowing harboring hydrophobic drugs via hydrogen bonding and hydrophobic interactions. CLSM also demonstrates that PSPG nanoparticles were simultaneously loaded with both DOX and nucleic acids. The green fluorescence signal from the fluorescein isothiocyanate (FITC)-labeled siRNA and the inherent red fluorescence signal from DOX were clearly visible within PSPG nanoparticles. The overlap of both signals yields yellow fluorescence in the field of vision, suggesting that both cargoes have been successfully encapsulated by PSPG polymers (Figure 4l–n).

We also used X-ray diffraction (XRD) and 2D nuclear overhauser effect spectroscopy (2D-NOESY) to confirm how DOX is encapsulated by PSPG polymers. Figure S6a (Supporting Information) shows the XRD patterns of free DOX, PSPG6, the physical mixture of DOX and PSPG6, and the supramolecular inclusion complex (SIC) formed by PSPG6 and DOX. The sharp reflections from DOX represent the channel-type crystal structure, whereas the broad peak of PSPG6 represents the amorphous character of the PSPG6 polymers. When DOX and PSPG6 were physically mixed without the SIC formation, the reflections derived from DOX were still clearly observed. However, when DOX formed the SIC with PSPG6 through the host–guest interaction, these reflections from DOX disappeared. This is a strong evidence of the amorphous structure of PSPG6, suggesting the SIC formation between PSPG6 and DOX. Furthermore, 2D-NOESY indicates that the proton from benzoic moiety of DOX (≈7.5 ppm) is well correlated with the inner protons of G2 or the G2 moieties of PSPG6 (1.89 and 2.17 ppm), indicating that DOX formed the SIC with PSPG6 (Figure S6b,c, Supporting Information).

All PSPG polymers shows good ability to complex with DNA or siRNA (Figure S7, Supporting Information). Complete DNA

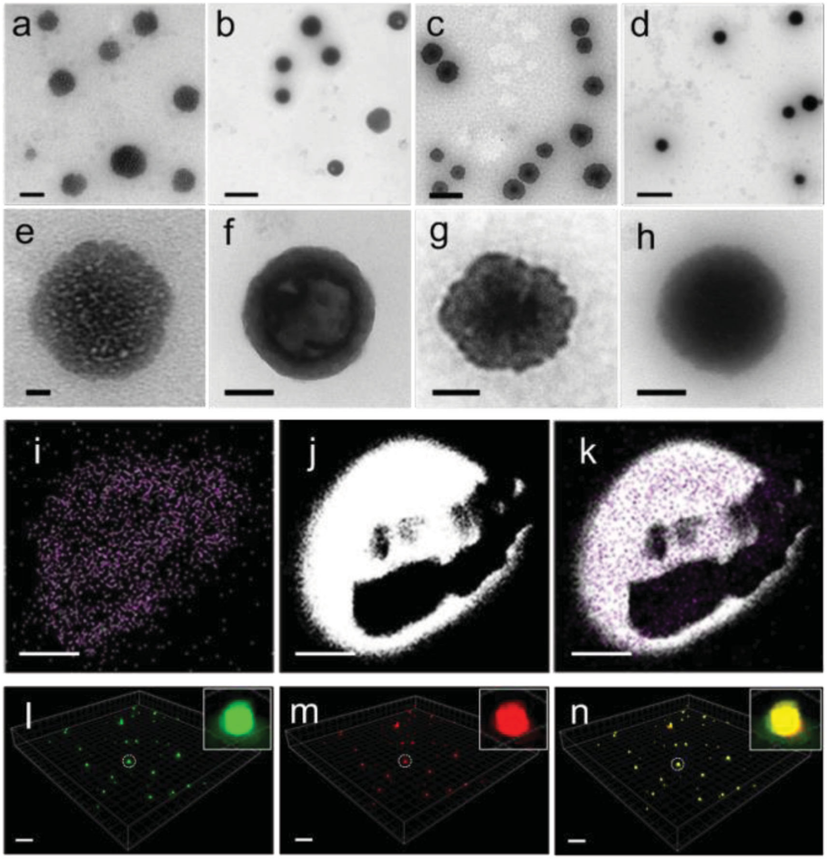

Figure 4. TEM images of a,e) PSPG6, b,f) PSPG6/DNA complexes, c,g) PSPG6/DOX3 complexes, and d,h) PSPG6/DOX3/DNA tertiary complexes. i) EDX elemental distribution of phosphorus from DNA, j) HAADF image of PSPG6/DNA complexes, and k) EDX elemental mapping of PSPG6/DNA complexes. l–n) Fluorescence images of PSPG6/DOX1/siRNA complexes acquired by CLSM microscope with a standard FITC/TRITC/DAPI filter set. FITC-labeled siRNA was visualized with the FITC filter, and the inherent red fluorescence of DOX was observed with the TRITC filter. Image (n) is the overlap image of (a) and (b). The scale bars represent a–d) 500 nm, e–h) 100 nm, i–k) 50 nm, and l–n) 15 μm, respectively.

complexation occurred at N/P ratio of 2, whereas slightly higher N/P ratio (N/P = 4) was required to completely inhibit siRNA migration in the case of PSPG2 and PSPG4. This suggests that PSPG polymers have strong abilities to complex either type of nucleic acid. Dynamic light scattering indicates that PSPG polymers are able to self-assemble into nanoparticles in the range of 100–300 nm with either DNA (Figure S8, Supporting Information) or siRNA (Figure S9, Supporting Information) except for PSPG2, which is probably due to the low amine density in the whole polymer networks. In contrast with G2 polyplexes, the surface charge of PSPG polyplexes generally stabilized at very low values in the range of 2–7 mV after the complexation with nucleic acids, which was regardless of N/P ratio. This phenomenon is caused by the neutral PEG networks that shield the surface charge of cationic PSPG6 polyplexes after the structure inversion.[49,50] Similar results in particle size and zeta potential were obtained when PSPG6 was applied to complex siRNA (Figure S9, Supporting Information). DOX loading amount ranging from 9% to 30% is simply tuned by controlling the feed ratio of DOX to PSPG polymers (**Figure 5**a), and DOX loading amount merely affects the particle size or zeta potential of PSPG6 polyplexes in a wide N/P ratio range (Figures S8 and S9, Supporting Information). In sharp contrast, the highest loading capacity of G2 dendrimer is only 10%, which is much lower than that of PSPG6 (30%). Heparin stability and zeta potential studies indicate that PSPG6 heparin stability is significantly enhanced as compared with G2 dendrimer due to the PEG-induced shielding effect, which may impair the interaction between PSPG polyplexes and heparin as demonstrated previously (Figure 5b,c).[49] Similar to those sheddable nanoparticles for nucleic acid delivery,[51–53] our study shows that when the disulfide bonds linking bPEG and G2 were cleaved by dithiothreitol (DTT), the zeta potential of PSPG6/DOX1/DNA increased from 2.5 to 14.1 mV. This suggests that the presence of redox reagents triggers the reduction-responsive degradation of PSPG6, forming unshielded nanoparticles by means of the exposure of positive amino groups.

As a result of cleavage of disulfide bonds, the imbedded cationic dendrimers detached from bPEG network expose and thus the cationic G2 surface may initiate a stronger association with the heparin, triggering DNA release from complexes. From the redox-responsive dissociation mechanism, it would be reasonable to assume that the smart PSPG6 polyplexes can be stably transported within blood following systemic injection. After being internalized, the exposure of cationic layer in the GSH-rich reduction environment can promote efficient release of DNA from the PSPG polyplexes following endosomal escape.[54] We also noticed that PSPG6 nanoparticles released DOX rapidly in the presence of 5×10^{-3} mol L^{-1} DTT, a reductive environment analogous to that of the intracellular compartments (Figure 5d). In contrast, marginal DOX release (<30%) was observed within 16 h for the non-redox-responsive analog PPG6 under the same conditions as well as for PGPS6 in the absence of DTT. These results suggest PSPG6 nanoparticles may efficiently release DOX at cytosol where GSH is rich after endosomal escape.

2.3. In Vitro Cytotoxicity and Transfection Activity

Recent studies demonstrates that cationic PAMAM dendrimers are able to bind the surface of cell membrane with high affinity and be internalized by endocytosis afterwards due to their small sizes and cationic nature.[55,56] The high level of glutathione in the cytosol are the triggers responsible for the degradation of reduction-sensitive polymers through thiol–disulfide exchange.[57] Therefore, PSPG polyplexes are expected to degrade inside the cells after being internalized

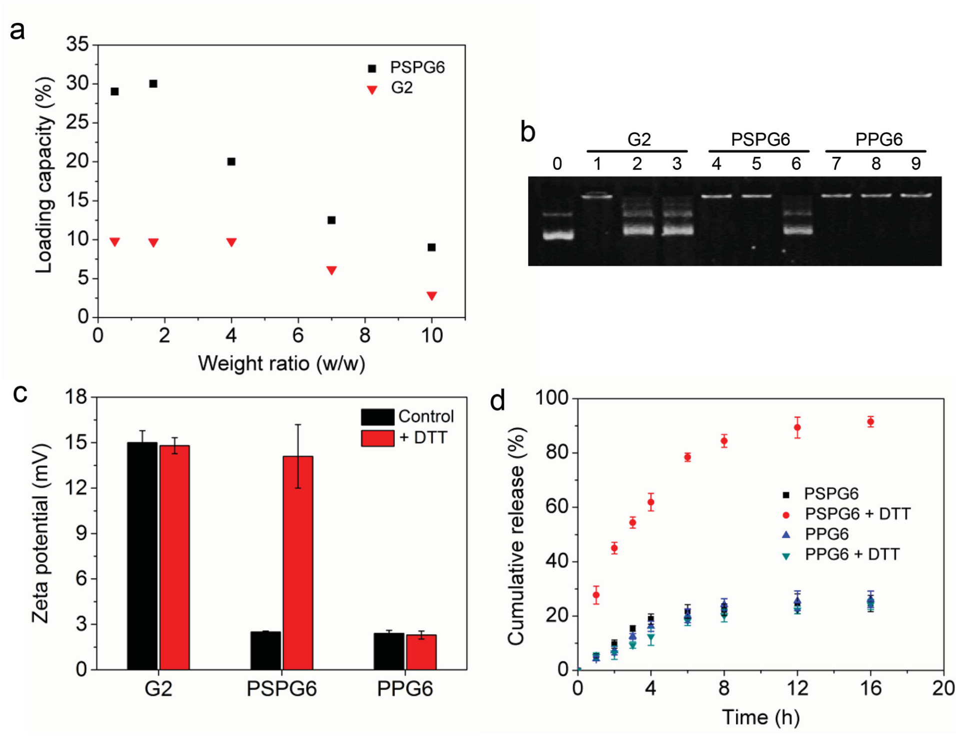

Figure 5. a) The DOX loading capacity of PSPG6 and G2 as a function of initial feed ratio of vector/DOX. b) Agarose gel electrophoresis retardation of pDNA complexed with G2, PSPG6, PPG6 at N/P of 10. The polymer/DNA complexes were treated in different conditions before gel electrophoresis. Conditions: Lane 1, 4, 7: 5×10^{-3} mol L^{-1} DTT; Lane 2, 5, 8: 420 µg mL^{-1} heparin; Lane 3, 6, 9: 5×10^{-3} mol L^{-1} DTT and 420 µg mL^{-1} DTT. Lane 0 is the band of pDNA only. c) Zeta potential of PSPG6/DOX1/DNA complexes at N/P ratio of 10 in the absence of 5×10^{-3} mol L^{-1} of DTT. The zeta potential of PSPG6/DOX1/DNA complexes in the absence of DTT and heparin was used as a control. d) Time-dependent release of DOX from PSPG6/DOX/DNA or PSP/DOX/DNA complexes in the presence or absence of 5×10^{-3} mol L^{-1} DTT. All quantitative data represent mean ± SD (*n* = 3).

due to the presence of disulfide bonds linking bPEG and G2 moieties. While all redox-responsive PSPG polymers shows negligible cytotoxicity in the polymer concentration range from 50 to 400 µg mL^{-1} after incubating with HEK293 cells for 4 or 24 h, non-redox-sensitive PPG4 and PPG6 polymers show time- and dose-dependent cytotoxicity (Figure S10, Supporting Information). Live/dead cell viability assay also further validates the low-cytotoxic nature of PSPG polymers at high polymer concentrations up to 400 µg mL^{-1} (Figure S11, Supporting Information). We further investigate whether the inhibition of GSH by buthionine sulphoximine (BSO) significantly affects the cytotoxicity of PSPG polyplexes. BSO is a specific γ-glutamylcysteine synthetase inhibitor that blocks the rate-limiting step of glutathione biosynthesis, and is well-documented to reduce GSH level by inhibiting GSH in HEK293 cell lines.[58] As compared with PSPG6 in the absence of BSO, we found that the cytotoxicity of PSPG6 significantly increased in the polymer concentration range from 200 to 1000 µg mL^{-1} in the presence of BSO, suggesting that disulfide bonds linking bPEG and G2 plays an important role in reducing the cytotoxicity of PSPG6 (**Figure 6**a). In the tested polymer concentration range, PSPG6 shows similar dose-independent cytotoxicity as G2, and displays much lower cytotoxicity when comparing with "gold standard" polyethyleneimine (PEI) of 25 kDa. These results indicate that the intracellular degradation is of paramount importance in reducing the cytotoxicity of PSPG polymers by avoiding accumulation of high molecular weight polycations inside cells. Additionally, the biocompatible PEG backbones not only renders a much lower relative amino density as compared to native G2 dendrimers, but has also imparted biocompatible characteristics to the cationic carriers.[50,59]

Gene transfection mediated by PSPG polymers was first screened on the basis of luciferase gene expression. It was found that luciferase expression of PSPG-mediated gene transfection was greatly dependent on the N/P ratio of the polyplexes (Figure S12, Supporting Information). Gene transfection ability of all PSPG polymers became optimal at N/P ratio of 10. PSPG6 showed most strong transfection ability among these PSPG polymers, which was comparable to that of 25 kDa PEI (Figure S13, Supporting Information). It was also found that the higher the loading amount of DOX, the poorer the transfection ability of PSPG6, which was probably associated with DOX-induced cytotoxicity (Figure S14, Supporting Information). The non-redox-responsive analog PPG6, however, shows much lower transfection activity as compared with PSPG6, probably owing to the poor DNA release from the carrier. The transfection ability of PSPG polymers was also confirmed by high level of GFP expression that was mediated by PSPG/pEGFP complexes (Figure S13, Supporting Information). The ability of PSPG polymers to deliver siRNA and induce gene silencing was further screened on the basis of GFP gene silencing in HEK293/GFP cells which stably express the GFP (Figure S15, Supporting Information). Among PSPG polymers, PSPG6 also allowed an exceptionally powerful gene silencing

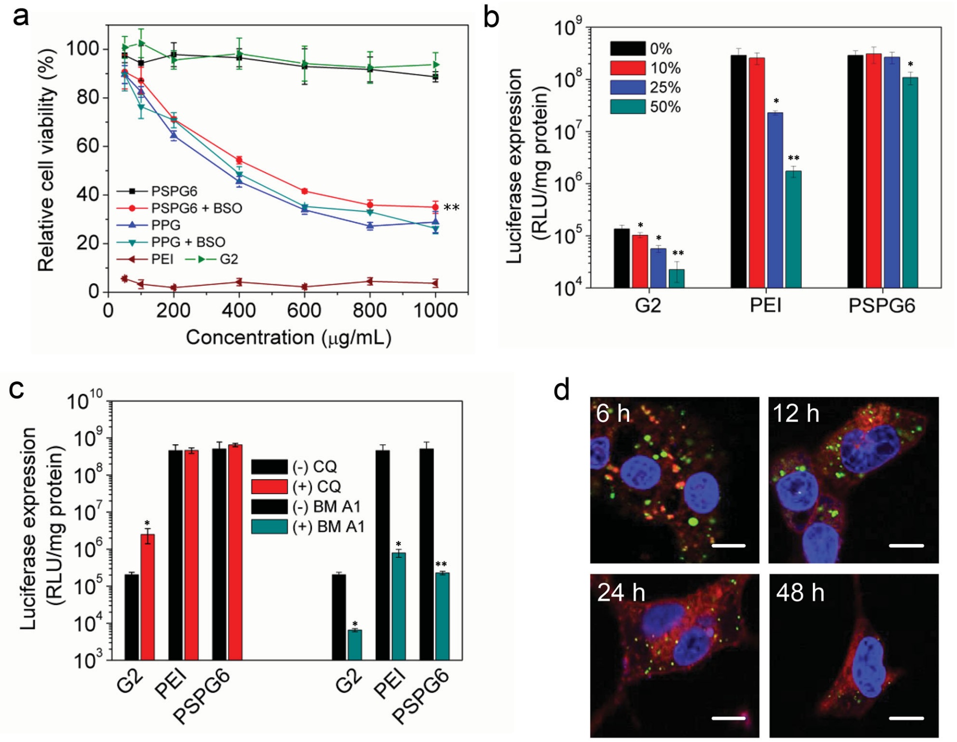

Figure 6. a) Cell viability of HEK293 cells treated with PSPG6 polymers at various concentrations in the absence or presence BSO (**$P < 0.01$, PSPG6 + BSO vs PSPG6). Non-redox-responsive PPG6, G2, and PEI (25 kDa) were used as controls. b) In vitro luciferase gene expression in HEK293 cells transfected with PSPG6 in different serum concentrations. Comparison of group means was made between serum-free group and serum-containing group. c) In vitro luciferase gene expression in HEK293 cells transfected with PSPG6 polyplexes at N/P ratio of 10 in the presence of chloroquine (CQ) or bafilomycin A1 (BM A1). Comparison of group means was made between the control group (without CQ or BM A1 treatment) and the group with CQ or BM A1 treatment. Data represent mean ± SD ($n = 3$, Student's t-test, *$P < 0.05$, **$P < 0.01$). d) Time-dependent in vitro fluorescence image of HEK293 cells transfected with PSPG6/DOX1/siRNA. siDNA was labeled with FITC. The scale bar represents 10 μm.

with the specific GFP siRNA, exhibiting up to 35% of GFP knockdown. Other PSPG polymers showed moderate gene silence ability. These results demonstrate that PSPG6 mediates a particularly efficient pDNA transfection and specific siRNA-based gene silencing.

2.4. In Vitro Serum Stability, Endosomal Escape Capability, and Cargo Release

We further examine whether serum stability can be improved in serum-rich conditions (Figure 6b). It is found that whereas the luciferase expression mediated by "gold standard" 25 kDa PEI and G2 dramatically decrease with the increasing concentration of serum, PSPG6 shows significantly enhanced serum stability, which is almost regardless of serum concentration. PEI-mediated luciferase expression in the presence of 50% FBS decreased by 165-fold as compared to that in serum-free condition, and similar trend was observed in the case of G2-mediated gene transfection. Nevertheless, PSPG6-mediated luciferase expression was merely affected by serum concentrations in the range of 10%–30%, and only slightly decreased in the presence of 50% FBS condition. In the high serum concentrations, PSPG6 shows 10–60 times much stronger transfection ability than PEI, suggesting enhanced antiserum ability due to the presence of PEG networks over the dendrimer surface.

The effect of chloroquine and bafilomycin A1 on gene transfection efficiency was investigated to examine whether endosomal escape capability of PSPG6 was enhanced as compared with G2 (Figure 6c). Chloroquine is well known to destabilize endosome by preventing endosomal acidification, thereby leading to swelling and bursting of endosomes. Therefore, the presence of chloroquine is able to enhance transfection ability of gene delivery carriers with poor endosome escape capability. It was found that the presence of chloroquine can significantly enhance the G2 luciferase expression by one magnitude, whereas almost no change in terms of luciferase expression in the cells transfected by PSPG6 or PEI. PEI is well known for its strong buffering capacity and endosomal escape capability, and previous study indicates that the presence of chloroquine has only marginal effects on transgene expression in HeLa cells.[60] As a result, the marginal effect of chloroquine on PSPG6-mediated gene expression demonstrates that the high transfection efficiency of PSPG6 is at least partially due to its strong buffering capacity. On the other hand, bafilomycin A1 is a V-type ATPase inhibitor that prevents the acidification of endosomes and thus the accumulation of gene vector in endo/lysosomes. It is indirectly used to correlate endosomal escape rate to the buffering capacity of gene carrier. Generally, the gene expression in all groups decreases after bafilomycin A1 treatment. The decrease in the transfection efficiency of PSPG6 polyplexes in the presence of bafilomycin A1 (2000-fold) is much greater than that of G2 (30-fold) in the same experiment condition, suggesting that the buffering capacity of PSPG6 is much stronger than that of G2. These results imply that increasing the number of surface primary amines by assembling low generation dendrimers could significantly enhance endosomal buffering capacity.[61,62] To explore cellular uptake and release of cargos from PSPG6 polymers, intracellular trafficking of PSPG6/DOX1/siRNA complexes and cargo release were visualized in HEK 293 cells using CLSM (Figure 6d). siRNA labeled with FITC was used as a model nucleic acid for this study. It was observed PSPG6/DOX1/siRNA complexes were internalized into HEK293 cell lines and accumulated in the periphery of the cell nucleus as indicated by both green and red fluorescence. Most importantly, DOX distributed in the nucleus and cytoplasm, and DOX fluorescence intensity gradually increased over 24 h, suggesting efficient intracellular DOX release. Green fluorescence intensity gradually became weak, which also indicates siRNA release and the subsequent action of gene expression. The nanoscaled particle size of PSPG6/DOX1/siRNA complexes may play an important role in promoting efficient cellular uptake, which would greatly improve therapeutic outcomes by accumulating themselves inside the targeted cells. Moreover, as a stimuli-responsive delivery system which release drugs locally within the tumor cells, PSPG6 nanoparticles are also expected to achieve improved bioavailability while reducing systemic exposure.

2.5. In Vivo Gene Transfection

The above results prompt us to further explore whether both DOX and pDNA can effectively reside within tumor after the intratumoral injection of PSPG6/DOX1/pDNA. **Figure 7**a displays time-dependent in vivo fluorescence images of BALB/c nude mice with SMMC-7721 xenografts after the intratumoral injection. As expected, in the case of free DOX and pDNA group, both green and red fluorescence signals in the tumor site decreased dramatically with time, becoming negligible 8 h postinjection. This suggests quick clearance of free DOX or pDNA, resulting in relatively short residence time at tumor site. In contrast, for PSPG6/DOX1/pDNA group, although both fluorescence signals in tumor site gradually faded, relatively high fluorescence intensity still could be acquired even at 24 h postinjection (Figure 7d and Figure S16, Supporting Information). This demonstrates that while free DOX and pDNA are rapidly cleared by blood, PSPG6/DOX1/pDNA shows enhanced retention within the tumor site. The enhanced retention effect mediated by PSPG6 may significantly facilitate drug delivery efficiency and gene transfection in vivo. As a result, we find whereas tumor-bearing mice that are treated with free DOX after 24 h shows almost no fluorescence in the tumor tissue sections, very strong red fluorescence can still be detectable within tumor tissues from the mice that are treated with PSPG/DOX1/pDNA formulation (Figure 7b). This also indicates that PSPG6/DOX1/pDNA formulation could be retained for a prolonged time at higher concentration at tumor tissue. Furthermore, the gene expression in tumor sites were also examined 48 h after intratumoral injection of PSPG6/pDNA and other complexes. As shown in Figure 7c, the administration of naked pDNA results in very low gene expression in tumor site, whereas PSPG6-mediated in vivo gene transfection shows much higher level of GFP expression at the tumor site. Non-redox-responsive analog PPG6 only also shows very low in vivo gene expression, which is probably related to inefficient pDNA release at tumor site. It is noted to mention that the PSPG6/DOX1/pDNA complexes exhibit comparable level of GFP expression at the tumor site as compared with PSPG6/pDNA complexes, suggesting that the low loading amount of DOX merely affects its transfection activity in vivo. These results were also validated by in vivo luciferase expression assay (Figure 7e). Collectively, these results strongly suggest that PSPG6 polymer is an efficient co-delivery vector to deliver nucleic acids both in vitro and in vivo.

2.6. In Vivo Co-Delivery of DOX and Bcl-2 siRNA for Tumor Inhibition

The Bcl-2 oncogene is overexpressed in 50%–70% of all human cancers, and the overexpression of Bcl-2 is considered to be one of the mechanisms by which tumor cells acquire resistance to apoptosis.[63,64] Inhibition of Bcl-2 enhances the sensitivity of cancer cells to standard therapies, thereby indicating the importance of this gene as a potential therapeutic target in various human cancers.[65,66] In this study, co-delivery of DOX and Bcl-2 siRNA which is able to downregulate Bcl-2 oncogene expression was explored to examine whether a synergistic effect against murine tumor models could be exerted. As indicated in **Figure 8**a, tumor growth is greatly inhibited after intratumoral injection with PSPG6/DOX1/Bcl-2 formulations. The average tumor volume of the mice administered with PSPG6/DOX1/Bcl-2 formulation is around 20 mm^3 on the 22th day since the first treatment, and the therapeutic effect is at least five times more potent than that treated with either PSPG6/DOX or PSPG6/siRNA nanoparticles. This demonstrates that DOX therapeutic outcomes can be maximized only when DOX and Bcl-2 siRNA is co-delivered by PSPG6 simultaneously. The study of final tumor weight also validates the effectiveness of PSPG6/DOX1/Bcl-2 formulations (Figure 8d). Furthermore, positron emission tomography (PET), which provides highly sensitive imaging modality for tumor diagnosis, is utilized to precisely measure the tumor volume as demonstrated in the previous study.[67] As shown in Figure 8b, the circled area denotes the tumor position and the red color area within circles represents the volume of tumors. The red color area decreased dramatically from control groups to PSPG/DOX1/Bcl-2 group and very weak red fluorescence was observed when the mice was co-administered with DOX and Bcl-2 siRNA mediated by PSPG6. These results suggest the most effective treatment against tumor growth can be achieved by co-delivering DOX and Bcl-2 siRNA. Concurrently, almost no change in the body weights of mice administered with different formulations was observed, indicating the low toxicity nature and minimal side effect of the PSPG/DOX1/Bcl-2 formulation via intratumoral injection (Figure 8c).

Cell apoptosis in the tumors were analyzed by hematoxylin and eosin (H&E) staining, Ki67 and terminal deoxynucleotidyl transferase dUTP nick end labeling (TUNEL) assay after treatment with various formulations (**Figure 9**). The H&E stained

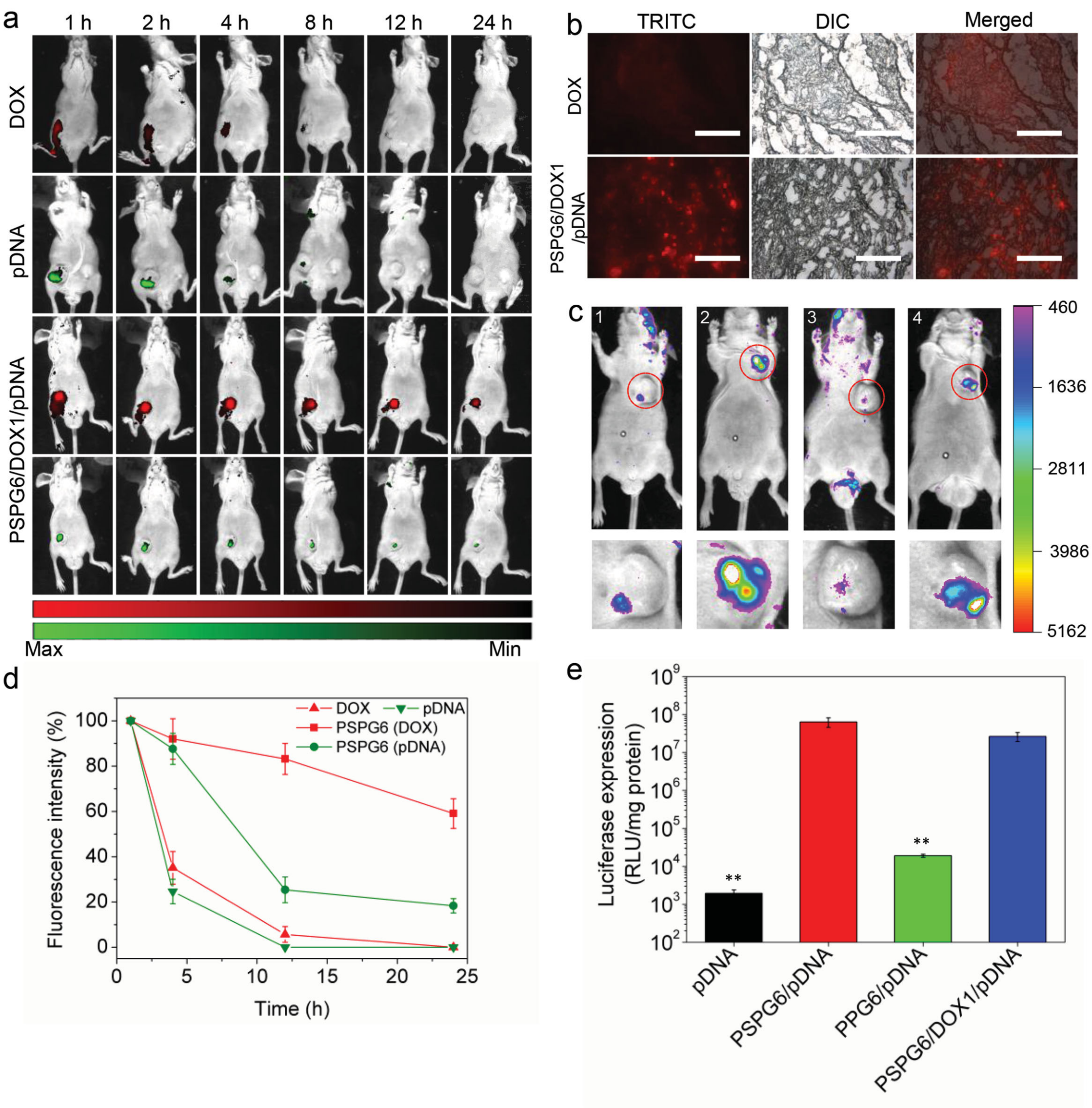

Figure 7. a) Time-dependent in vivo fluorescence imaging of tumor-bearing mouse treated with DOX, pDNA, or PSPG6/DOX1/pDNA complexes; b) fluorescence and white light images of tumor sections from murine tumor models treated with DOX or PSPG6/DOX1/pDNA 24 h after intratumoral injection. The scale bars represent 100 µm; c) fluorescence images at the tumor site of tumor-bearing BALB/c mice 48 h after intratumoral injection of pDNA alone (C1), PSPG6/pDNA (C2), PPG/pDNA (C3), and PSPG6/DOX2/pDNA (C4).The pDNA encoding green fluorescence protein (GFP) was used for this study. The fluorescence image in the lower panel corresponds to the cycled area in the tumor site of the mouse in the upper image; d) region of interest (ROI) analysis of time-dependent fluorescence intensity in tumor-bearing mouse treated with different formulations. Data represent mean ± SD ($n = 3$). The fluorescence intensity was expressed as a percentage of control, which is the absolute fluorescence intensity of ROI at 1 h in each group; e) in vivo luciferase gene expression in tumor transfected with different polymer/pGL3-Luc complexes at N/P ratios of 30. Comparison of group means was made between PSPG6/pDNA and other group. The results are expressed as mean ± SD ($n = 3$) (Student's *t*-test, $^{**}P < 0.01$).

sections of tumor tissues from phosphate buffered saline (PBS) and B-cell lymphoma 2 (Bcl-2) groups appeared to be most hypercellular and showed more obviously the nuclear polymorphism. Among these therapeutic groups, the tumor tissues from the treatment with the PSPG/DOX1/Bcl-2 formulation shows the fewest tumor cells and the highest level of tumor necrosis. The TUNEL and Ki67 assay also shows that co-delivery of DOX and Bcl-2 siRNA with PSPG6 can induce much more TUNEL-positive cells, and markedly reduce the percentage of proliferating Ki67-positive tumor cells, indicating the enhanced efficiency of treatments in inhibiting the proliferation and inducing apoptosis of tumor cells. These results demonstrate the effectiveness of PSPG6/DOX1/Bcl-2 formulation in vivo. Analysis of tumor tissues Bcl-2 protein staining reveals a distinct decrease in the protein density of the tumor slice after the co-delivery of DOX and Bcl-2, when compared with the PSPG6/DOX, PSPG6/Bcl-2, and other formulations (Figure 9, Figure S17, Supporting Information). These results of in vivo antitumor efficacy of co-delivery treatment strongly suggest that co-delivery of DOX and Bcl-2 siRNA exert a

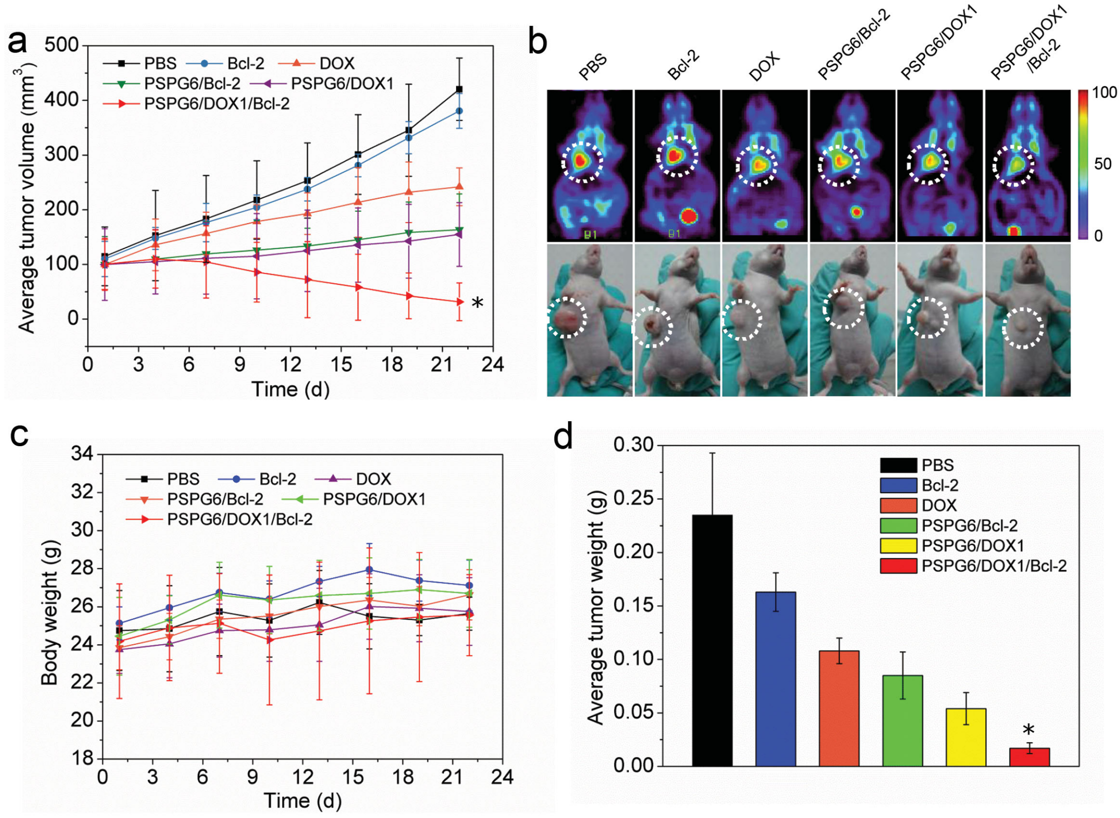

Figure 8. a) Inhibition of tumor growth in BALB/c nude mice with SMMC-7721 xenografts treated with PSPG6/DOX1/Bcl-2 and other formulations. Data represent mean ± SD ($n = 6$, Student's t-test, $^*P < 0.05$, PSPG6/DOX1 (or PSPG6/Bcl-2) vs PSPG6/DOX1/Bcl-2); b) PET images of in vivo tumor growth 22 d after the first treatment. The intensity is shown by the legend to the right; c) average body weights of tumor-bearing mice injected with the different formulations; d) the weight of tumor tissues dissected from mice 22 d later after the first treatment. Data represent mean ± SD ($n = 6$, Student's t-test, $^*P < 0.05$, PSPG6/DOX1(or PSPG6/Bcl-2) vs PSPG6/DOX1/Bcl-2).

combinational effect against tumor growth in murine tumor models. The evidence also demonstrates that PSPG6 plays an important role as an efficient co-delivery vector for the cancer treatment in vivo.

3. Conclusions

In conclusion, we have developed structure-invertible nanoparticles PSPG6 to serve as redox-responsive carriers for the efficient co-delivery of hydrophobic drugs and nucleic acids in this work. This vector bears a branched PEG in the interior and six low generation dendrimers at the terminals, which are linked by redox-responsive disulfide bonds. PSPG6 polymer is capable of simultaneously loading both hydrophobic drugs and nucleic acids, and shows high drug loading capacity through structure inversion. PSPG6 also exhibits improved serum stability and enhanced endosomal escape capability as compared with unmodified low generation dendrimers. The cleavage of disulfide linkages significantly decreases the cytotoxicity, and promotes more efficient drug release and gene transfection both in vitro and in vivo. Co-delivery of DOX and Bcl-2 siRNA exerts a combinational effect on the inhibition of tumor growth, which is much more effective than either DOX- or Bcl-2 siRNA-based monotherapy. This multifunctional co-delivery nanoparticle opens up new possibilities for exploring a wide range of applications in combination therapies at the dawning era of personalized nanomedicine for cancer therapy.

4. Experimental Section

A full description of the methods is provided in the Supporting Information.

Materials: 1,4-butanediamine, cystamine dihydrochloride, NHS-PEG-OH (2000 Da), branched PEG with eight arms (15 000 Da), 1-(3-dimethylaminopropyl)-3-ethylcarbodiimide hydrochloride (EDCI), 1-hydroxy-7-azabenzotriazole (HOAt), *tert*-butyl(2-aminoethyl) carbamate, $NaBH_4$, $NiCl_2{\cdot}6H_2O$, trifluoroacetic acid (TFA), triethylamine (Et_3N), CDI, branched PEI with molecular weight of 25 KDa, DTT, doxorubicin hydrochloride, 3-(4,5-dimethylthiazol-2-yl)-2,5-diphenyltetrazolium bromide (MTT) were purchased from Sigma-Aldrich (USA). 2-(4-amidinophenyl)-6-indolecarbamidine dihydrochloride (DAPI), lyso-tracker red, live/dead viability/cytotoxicity assay kit, unlabeled negative control siRNA, 5′-carboxyfluorescein (FAM)-labeled negative control siRNA and GFP siRNA (GFP-22) were purchased from Life Technologies (Grand Island, USA). The pDNA encoding firefly luciferase (pGL3-Luc) and green fluorescent protein (pEGFP) were purchased from Promega (Madison, USA). Solvents were used as received. Dialysis membranes were purchased from Spectrum Labs (Rancho Dominguez, USA).

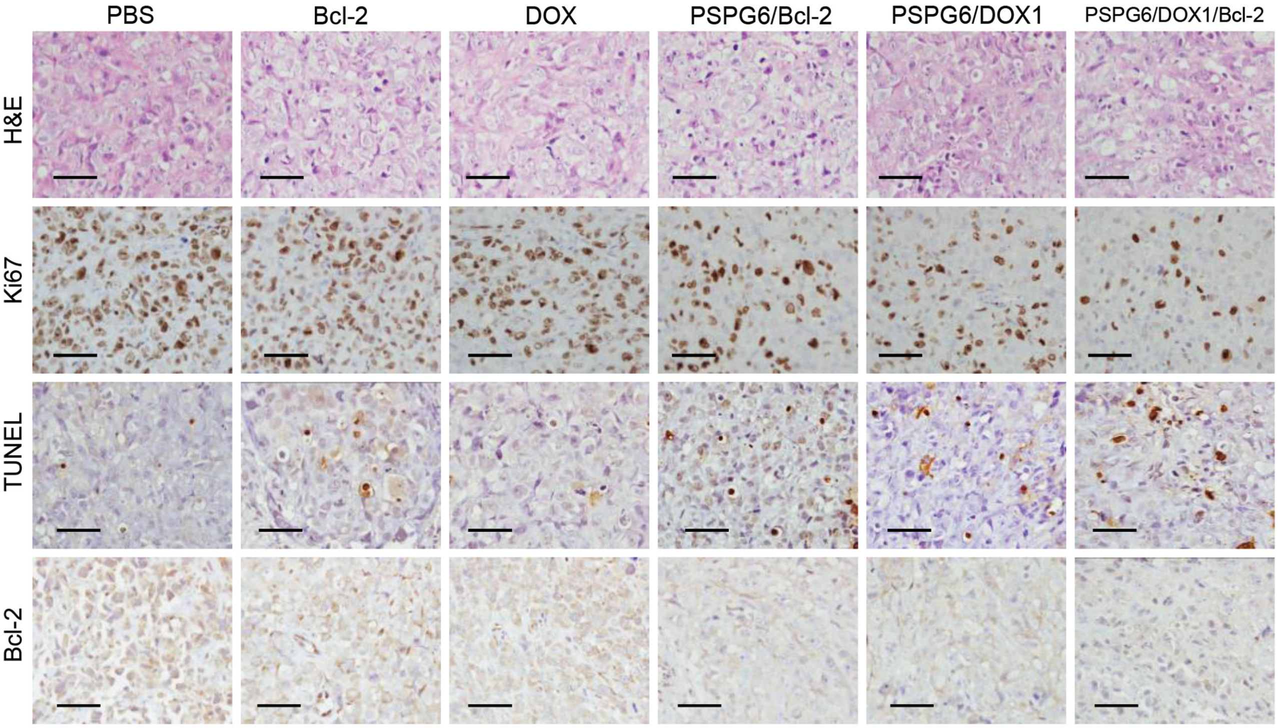

Figure 9. H&E, Ki67, TUNEL, and Bcl-2 protein analysis of tumor tissues of BALB/c nude mice with SMMC-7721 xenografts after treatment with various formulations. All scale bars represent 20 μm.

Cell Culture: All cell lines used in this study were purchased from American Type Culture Collection (ATCC, Rockville, MD). Human embryonic kidney 293 cell lines HEK293, HEK293 and GFP-expressing HEK293 cells (HEK293-GFP) were cultured in Dulbecco's modified eagle medium (DMEM) containing 10% fetal calf serum (FCS). Human liver cancer SMMC-7721 cell line was cultured in RPMI 1640 culture medium containing 10% FCS. The cells were grown under humidified air containing 5% CO_2 at 37 °C.

Animal Models: Animal experiments were performed in accordance with the CAPN (China Animal Protection Law), and protocols were approved by Zhejiang University Animal Care and Use Committee. Athymic female mice (BALB/c strain) (four weeks, 15–18 g weight) were purchased from the Zhejiang University Animal Care Center and maintained in a pathogen-free environment under controlled temperature (25 °C).

General Characterization: The ^{1}H NMR spectra of samples were recorded on a Bruker DRX-400 spectrometer (Bruker, Ettlingen, Germany) at 400 MHz at room temperature. The ATR-FTIR spectra of PSPG6 and PSPG6/DOX/DNA were analyzed by attenuated total-reflection Fourier transformed infrared spectroscopy (Varian, Excalibur, USA). The surface chemical structure of PSPG6 and PSPG6/DOX/DNA were determined by XPS (Physical Electronics PHI 5802). Energy dispersive X-ray spectroscopy profiles were acquired by using a FEI Tecnai TF20 instrument with an operation voltage of 200 kV. The number-average and weight-average molecular mass (M_w) of PSPG6 were analyzed by a Waters 515 gel permeation chromatography (GPC) equipped with the TSK-GEL G4000PWXL column (TOSOH, Japan) and 2410 differential refractive index detector (Waters, Milford, MA, USA). The morphology of complexes was examined by transmission electron microscope (HT7700, Hitachi). The confocal images were acquired on a CLSM (Radiance 2100, Bio-Rad).

Statistical Analysis: All experiments were repeated at least three times. Data are presented as means ± standard deviation. Statistical significance ($p < 0.05$ or $p < 0.01$) was evaluated by using Student's t-test when only two groups were compared. In all tests, statistical significance was set at $p < 0.05$.

Supporting Information

Supporting Information is available from the Wiley Online Library or from the author.

Acknowledgements

K.W., Q.H., Y.P., and G.T. designed research; K.W., Q.H., and Y.P. performed research; K.W., W.Z., and Y.P. analyzed data; M.Z. helped antitumor efficacy study in vivo; Y.P. and G.T. supervised the whole project and wrote the paper. The authors greatly acknowledge National Natural Science Foundation of China for the financial support of this work (Project No. 21374098).

Received: November 6, 2014
Revised: March 25, 2015

---

[1] M. M. Janat-Amsbury, J. W. Yockman, M. Lee, S. Kern, D. Y. Furgeson, M. Bikram, S. W. Kim, *Mol. Ther.* **2004**, *9*, 829.
[2] Y. Wang, S. Gao, W. H. Ye, H. S. Yoon, Y. Y. Yang, *Nat. Mater.* **2006**, *5*, 791.
[3] N. Wiradharma, Y. W. Tong, Y. Y. Yang, *Biomaterials* **2009**, *30*, 3100.
[4] Q. D. Hu, H. Fan, Y. Ping, W. Q. Liang, G. P. Tang, J. Li, *Chem. Commun.* **2011**, *47*, 5572.
[5] L. Y. Qiu, Y. H. Bae, *Biomaterials* **2007**, *28*, 4132.

[6] V. Tsouris, M. K. Joo, S. H. Kim, I. C. Kwon, Y. Y. Won, *Biotechnol. Adv.* **2014**, *32*, 1037.
[7] K. Han, S. Chen, W. H. Chen, Q. Lei, Y. Liu, R. X. Zhuo, X. Z. Zhang, *Biomaterials* **2013**, *34*, 4680.
[8] H. Yu, Z. Xu, X. Chen, L. Xu, Q. Yin, Z. Zhang, Y. Li, *Macromol. Biosci.* **2014**, *14*, 100.
[9] C. H. Zhu, S. Jung, S. B. Luo, F. H. Meng, X. L. Zhu, T. G. Park, Z. Y. Zhong, *Biomaterials* **2010**, *31*, 2408.
[10] F. Zhao, H. Yin, J. Li, *Biomaterials* **2014**, *35*, 1050.
[11] Q.-D. Hu, G.-P. Tang, P. K. Chu, *Acc. Chem. Res.* **2014**, *47*, 2017.
[12] Q. Hu, W. Li, X. Hu, J. Shen, X. Jin, J. Zhou, G. Tang, P. K. Chu, *Biomaterials* **2012**, *33*, 6580.
[13] Q. D. Hu, H. Fan, Y. Ping, W. Q. Liang, G. P. Tang, J. Li, *Chem. Commun.* **2011**, *47*, 5572.
[14] H. Fan, Q. D. Hu, F. J. Xu, W. Q. Liang, G. P. Tang, W. T. Yang, *Biomaterials* **2012**, *33*, 1428.
[15] D. Li, Y. Li, H. Xing, J. Guo, Y. Ping, G. Tang, *Adv. Funct. Mater.* **2014**, *24*, 5482.
[16] W. Xiao, X. Chen, L. Yang, Y. Mao, Y. Wei, L. Chen, *Int. J. Pharm.* **2010**, *393*, 119.
[17] H. Wang, P. Zhao, W. Su, S. Wang, Z. Liao, R. Niu, J. Chang, *Biomaterials* **2010**, *31*, 8741.
[18] Y. Chen, S. R. Bathula, J. Li, L. Huang, *J. Biol. Chem.* **2010**, *285*, 22639.
[19] A. M. Chen, M. Zhang, D. Wei, D. Stueber, O. Taratula, T. Minko, H. He, *Small* **2009**, *5*, 2673.
[20] H. Meng, M. Liong, T. Xia, Z. Li, Z. Ji, J. I. Zink, A. E. Nel, *ACS Nano* **2010**, *4*, 4539.
[21] X. Ma, Y. Zhao, K. W. Ng, Y. Zhao, *Chem. Eur. J.* **2013**, *19*, 15593.
[22] Y. Ren, C. S. Kang, X. B. Yuan, X. Zhou, P. Xu, L. Han, G. X. Wang, Z. Jia, Y. Zhong, S. Yu, J. Sheng, P. Y. Pu, *J. Biomater. Sci. Polym. Ed.* **2010**, *21*, 303.
[23] M. Han, Q. Lv, X.-J. Tang, Y.-L. Hu, D.-H. Xu, F.-Z. Li, W.-Q. Liang, J.-Q. Gao, *J. Control. Release* **2012**, *163*, 136.
[24] L. Han, R. Huang, J. Li, S. Liu, S. Huang, C. Jiang, *Biomaterials* **2011**, *32*, 1242.
[25] S. Biswas, P. P. Deshpande, G. Navarro, N. S. Dodwadkar, V. P. Torchilin, *Biomaterials* **2013**, *34*, 1289.
[26] J. M. Li, Y. Y. Wang, M. X. Zhao, C. P. Tan, Y. Q. Li, X. Y. Le, L. N. Ji, Z. W. Mao, *Biomaterials* **2012**, *33*, 2780.
[27] Y. Xiao, R. Jaskula-Sztul, A. Javadi, W. Xu, J. Eide, A. Dammalapati, M. Kunnimalaiyaan, H. Chen, S. Gong, *Nanoscale* **2012**, *4*, 7185.
[28] Z. J. Deng, S. W. Morton, E. Ben-Akiva, E. C. Dreaden, K. E. Shopsowitz, P. T. Hammond, *ACS Nano* **2013**, *7*, 9571.
[29] M. A. Quadir, R. Haag, *J. Control. Release* **2012**, *161*, 484.
[30] Q. Xu, C. H. Wang, D. W. Pack, *Curr. Pharm. Des.* **2010**, *16*, 2350.
[31] Y. Cheng, L. Zhao, Y. Li, T. Xu, *Chem. Soc. Rev.* **2011**, *40*, 2673.
[32] H. Liu, H. Wang, W. Yang, Y. Cheng, *J. Am. Chem. Soc.* **2012**, *134*, 17680.
[33] Y. Cheng, Y. Li, Q. Wu, J. Zhang, T. Xu, *Eur. J. Med. Chem.* **2009**, *44*, 2219.
[34] S. H. Medina, M. E. El-Sayed, *Chem. Rev.* **2009**, *109*, 3141.
[35] Y. Wang, W. Kong, Y. Song, Y. Duan, L. Wang, G. Steinhoff, D. Kong, Y. Yu, *Biomacromolecules* **2009**, *10*, 617.
[36] H. M. Wu, S. R. Pan, M. W. Chen, Y. Wu, C. Wang, Y. T. Wen, X. Zeng, C. B. Wu, *Biomaterials* **2011**, *32*, 1619.
[37] A. Harada, Y. Kimura, C. Kojima, K. Kono, *Biomacromolecules* **2010**, *11*, 1036.
[38] A. Kumar, V. K. Yellepeddi, G. E. Davies, K. B. Strychar, S. Palakurthi, *Int. J. Pharm.* **2010**, *392*, 294.
[39] A. Akbarzadeh, R. Rezaei-Sadabady, S. Davaran, S. W. Joo, N. Zarghami, Y. Hanifehpour, M. Samiei, M. Kouhi, K. Nejati-Koshki, *Nanoscale Res. Lett.* **2013**, *8*, 102.
[40] S. Kim, Y. Shi, J. Y. Kim, K. Park, J. X. Cheng, *Expert Opin. Drug Delivery* **2010**, *7*, 49.
[41] Q. D. Hu, G. P. Tang, P. K. Chu, *Acc. Chem. Res.* **2014**, *47*, 2017.
[42] F. Tang, L. Li, D. Chen, *Adv. Mater.* **2012**, *24*, 1504.
[43] H. Wang, M. Xu, Z. Wu, W. Zhang, J. Ji, P. K. Chu, *ACS Appl. Mater. Interfaces* **2012**, *4*, 4380.
[44] Q. Wang, W. Jin, G. Wu, Y. Zhao, X. Jin, X. Hu, J. Zhou, G. Tang, P. K. Chu, *Biomaterials* **2014**, *35*, 479.
[45] L. Wan, Y. You, Y. Zou, D. Oupicky, G. Mao, *J. Phys. Chem. B* **2009**, *113*, 13735.
[46] S. Mao, M. Neu, O. Germershaus, O. Merkel, J. Sitterberg, U. Bakowsky, T. Kissel, *Bioconjugate Chem.* **2006**, *17*, 1209.
[47] B. J. Rackstraw, A. L. Martin, S. Stolnik, C. J. Roberts, M. C. Garnett, M. C. Davies, S. J. B. Tendler, *Langmuir* **2001**, *17*, 3185.
[48] J. M. Frechet, *Proc. Natl. Acad. Sci. U. S. A.* **2002**, *99*, 4782.
[49] Y. Ping, Q. Hu, G. Tang, J. Li, *Biomaterials* **2013**, *34*, 6482.
[50] Y. Ping, C. D. Liu, Z. X. Zhang, K. L. Liu, J. H. Chen, J. Li, *Biomaterials* **2011**, *32*, 8328.
[51] S. Takae, K. Miyata, M. Oba, T. Ishii, N. Nishiyama, K. Itaka, Y. Yamasaki, H. Koyama, K. Kataoka, *J. Am. Chem. Soc.* **2008**, *130*, 6001.
[52] X. Z. Yang, J. Z. Du, S. Dou, C. Q. Mao, H. Y. Long, J. Wang, *ACS Nano* **2012**, *6*, 771.
[53] C. Zhu, M. Zheng, F. Meng, F. M. Mickler, N. Ruthardt, X. Zhu, Z. Zhong, *Biomacromolecules* **2012**, *13*, 769.
[54] K. Remaut, B. Lucas, K. Braeckmans, J. Demeester, S. C. De Smedt, *J. Control. Release* **2007**, *117*, 256.
[55] L. Albertazzi, M. Serresi, A. Albanese, F. Beltram, *Mol. Pharmaceutics* **2010**, *7*, 680.
[56] F. P. Seib, A. T. Jones, R. Duncan, *J. Control. Release* **2007**, *117*, 291.
[57] F. H. Meng, W. E. Hennink, Z. Zhong, *Biomaterials* **2009**, *30*, 2180.
[58] T. W. Sedlak, M. Saleh, D. S. Higginson, B. D. Paul, K. R. Juluri, S. H. Snyder, *Proc. Natl. Acad. Sci. U. S. A.* **2009**, *106*, 5171.
[59] D. Li, Y. Ping, F. J. Xu, H. Yu, H. M. Pan, H. L. Huang, Q. Q. Wang, G. P. Tang, J. Li, *Biomacromolecules* **2010**, *11*, 2221.
[60] N. P. Gabrielson, D. W. Pack, *J. Control. Release* **2009**, *136*, 54.
[61] L. Albertazzi, F. M. Mickler, G. M. Pavan, F. Salomone, G. Bardi, M. Panniello, E. Amir, T. Kang, K. L. Killops, C. Bräuchle, R. J. Amir, C. J. Hawker, *Biomacromolecules* **2012**, *13*, 4089.
[62] J. Zhou, J. Wu, N. Hafdi, J.-P. Behr, P. Erbacher, L. Peng, *Chem. Commun.* **2006**, *14*, 2362.
[63] R. J. Youle, A. Strasser, *Nat. Rev. Mol. Cell Biol.* **2008**, *9*, 47.
[64] S. Shimizu, T. Kanaseki, N. Mizushima, T. Mizuta, S. Arakawa-Kobayashi, C. B. Thompson, Y. Tsujimoto, *Nat. Cell Biol.* **2004**, *6*, 1221.
[65] Y. Tabuchi, J. Matsuoka, M. Gunduz, T. Imada, R. Ono, M. Ito, T. Motoki, T. Yamatsuji, Y. Shirakawa, M. Takaoka, M. Haisa, N. Tanaka, J. Kurebayashi, V. C. Jordan, Y. Naomoto, *Int. J. Oncol.* **2009**, *34*, 313.
[66] K. Tanabe, R. Kim, H. Inoue, M. Emi, Y. Uchida, T. Toge, *Int. J. Oncol.* **2003**, *22*, 875.
[67] Q. Hu, M. Wu, C. Fang, C. Cheng, M. Zhao, W. Fang, P. K. Chu, Y. Ping, G. Tang, *Nano Lett.* **2015**, *15*, 2732.
